Research Square

Preprints are preliminary reports that have not undergone peer review.
They should not be considered conclusive, used to inform clinical practice,
or referenced by the media as validated information.

Anisotropic Behavior and Micromechanisms of Ti60 Alloy Sheet

Shao Yanxin
Shenyang Aerospace University
Hui Zheng
Shenyang Aerospace University
Yongliang Zhang
Shenyang Aircraft Industry (Group) Co., Ltd.
Jue Wang
Shenyang Aircraft Industry (Group) Co., Ltd.
Yingjie Han
Shenyang Aircraft Industry (Group) Co., Ltd.
Tianzhang Zhao
tzzhao@alum.imr.ac.cn
Shenyang Aerospace University
Yingwei Qi
Shenyang Aerospace University
Yiqiang Mu
Shenyang Aerospace University

Research Article

Keywords: Ti60 sheet, Anisotropy, Texture effect, Schmid factors, CRSS

Posted Date: April 21st, 2026

DOI: https://doi.org/10.21203/rs.3.rs-9353080/v1

License: This work is licensed under a Creative Commons Attribution 4.0 International License.
Read Full License

Additional Declarations: No competing interests reported.

Version of Record: A version of this preprint was published at International Journal of Material Forming on June 1st, 2026. See the published version at https://doi.org/10.1007/s12289-026-02038-2.

Anisotropic Behavior and Micromechanisms of Ti60 Alloy Sheet

Shao Yanxin[1], Hui Zheng[1], Yongliang Zhang[2], Jue Wang[2], Yingjie Han[2], Tianzhang Zhao[1*], Yingwei Qi[1], Yiqiang Mu[1]

[1*] Shenyang Aerospace University, Shenyang, 110136, Liaoning Province, China.

[2]Shenyang Aircraft Industry (Group) Co., Ltd.,110034, Liaoning Province, China.

*Corresponding author(s). E-mail(s): tzzhao@alum.imr.ac.cn;

Abstract

The mechanical anisotropy of near-α titanium alloys under high-temperature service conditions plays a critical role in determining their formability and structural reliability. In this study, a Ti60 rolled plate was selected as the research material, and the evolution of tensile anisotropy along the RD, TD, and DD was systematically investigated at room temperature and within the temperature range of 720-840°C. The results reveal that the anisotropy of yield strength in the Ti60 plate can be divided into three distinct stages. At room temperature, the yield strengths along the TD and RD are comparable and higher than that along the DD, following the order TD>RD>DD. In the intermediate temperature range of 720-780°C, the yield strengths along the RD and DD become comparable and are lower than that along the TD, maintaining the same ranking of TD>RD>DD. At 840°C, the yield strengths along the TD and RD become comparable, while the anisotropy exhibits a reversal, following the order DD>RD>TD. Based on texture data obtained from EBSD analysis, the distributions and average values of the Schmid factors for the primary slip systems along the three directions were calculated. Combined with the temperature-dependent variations in the critical resolved shear stress (CRSS) of different slip systems, a slip activity parameter was introduced to quantitatively elucidate the origins of mechanical anisotropy. The results indicate that at room temperature, plastic deformation is primarily governed by prismatic slip and basal slip, together with non-thermally activated path-controlled mechanisms, which collectively influence the anisotropic behavior of the titanium alloy. The ranking of slip activity, DD>RD>TD, provides a reasonable explanation for the observed yield strength anisotropy at room

temperature. In the intermediate temperature range of 720-780°C, plastic deformation becomes increasingly dependent on thermally activated dislocation slip, and the yield strength exhibits a strong negative correlation with slip activity. Although the CRSS values of various slip systems decrease significantly, their rates of reduction differ, leading to the concurrent activation of multiple $\langle \boldsymbol{a} \rangle$-type slip systems and resulting in the yield strength along the RD decreasing to a level comparable to that along the DD. When the temperature reaches 840°C, the dominant deformation mechanism undergoes a fundamental transition, shifting to grain boundary sliding-dominated deformation accompanied by the simultaneous activation of multiple dislocation slip systems, which ultimately leads to the reversal of yield strength anisotropy at 840°C.

Keywords: Ti60 sheet, Anisotropy, Texture effect, Schmid factors, CRSS

1 Introduction

The rapid advancement of aerospace technology has imposed increasingly stringent requirements on the overall performance of materials used in critical hot-end components of aircraft[1, 2]. As a near-α high-temperature titanium alloy, Ti60 achieves excellent high-temperature strength, creep resistance, and microstructural stability through multicomponent alloying–induced solid-solution strengthening and dispersion strengthening from precipitated phases, and is therefore widely used in aero-engine components such as blades, disks, and drums[3–5].

Extensive studies have been carried out worldwide on the relationship between the mechanical behavior and microstructure of high-temperature titanium alloys. A large body of research has focused on alloy composition optimization, the influence of heat treatment schedules on microstructure and mechanical properties, as well as the evaluation of oxidation resistance, creep, and fatigue performance[6–9]. In addition, numerical simulations and advanced data-driven approaches have also been employed to predict and analyze the deformation behavior of high-temperature titanium alloys [10, 11]. To satisfy the aerodynamic shape and assembly requirements of complex components, titanium alloy sheets have become an important material form for structural applications[12]. However, after rolling, the grains within the sheet tend to develop strong preferred orientations, namely crystallographic texture, which results in pronounced anisotropy in the macroscopic mechanical properties of the material[13, 14]. When attention is specifically directed to the anisotropic behavior of Ti60 sheets under high-temperature conditions, the existing studies remain limited. On the one hand, most existing studies on the anisotropy of Ti60 sheets have focused on annealed materials[15–17], or have been limited to investigations at a single temperature of 600°C[18], resulting in a lack of systematic understanding of the anisotropic behavior of Ti60 under high-temperature conditions. On the other hand, existing studies generally characterize anisotropy by comparing only the rolling direction (RD) and the transverse direction (TD)[18–20], while the diagonal direction (DD), which is oriented at 45° to the rolling direction, is often neglected. However, in practical components, owing to the complexity of the stress state, the diagonal direction often constitutes one of the

critical load-bearing paths[21]. For engine components operating under complex stress states, inadequate consideration of material anisotropy during the design stage may lead to premature failure in service, potentially resulting in severe consequences[22–24]. Temperature is a key variable influencing anisotropic behavior. At room temperature, plastic deformation in titanium alloys is primarily governed by dislocation slip, and the resulting anisotropy is mainly controlled by the relative ease of activation of basal $\langle a \rangle$ and prismatic $\langle a \rangle$ slip systems, which is closely associated with the initial crystallographic texture[25, 26]. However, with increasing temperature, the deformation mechanisms become more complex, and the activation of pyramidal $\langle c+a \rangle$ slip becomes increasingly easier; the contribution of grain boundary sliding may gradually become significant[27, 28]; dynamic recovery and recrystallization processes can also facilitate deformation coordination and softening[29, 30]. The activation and competition among these high-temperature deformation mechanisms inevitably exert a profound influence on both the manifestation and the magnitude of material anisotropy.

Based on the above research background and analysis, this study focuses on Ti60 high-temperature titanium alloy sheets, aiming to systematically reveal the anisotropic evolution of tensile mechanical properties from room temperature to elevated temperatures (with particular focus on 700-900°C), and to further elucidate the underlying microstructural and physical mechanisms. In this study, the anisotropic behavior of the material is investigated under four temperature conditions along three loading directions, namely the rolling direction (RD), transverse direction (TD), and diagonal direction (DD). By integrating multiscale characterization methods, including macroscopic mechanical property testing, microstructural observation, texture analysis, and Schmid factor calculations of slip systems, the intrinsic relationships among macroscopic properties, crystallographic texture, and deformation mechanisms are established. Moreover, the evolution of anisotropy and its dominant mechanisms under the coupled effects of texture and temperature are clarified, thereby providing reliable theoretical guidance and experimental data support for the precise design and safe application of Ti60 sheets in key aero-engine components.

2 Experimental Method

2.1 Specimen Preparation

The experimental material used in this study was a Ti60 rolled sheet (Ti-5.7Al-4.0Sn-3.5Zr-0.9Mo-0.4Nb-1.0Ta-0.4Si-0.06C (wt%), β-transus temperature: 1050°C) with a thickness of 1.6 mm. The test specimens were prepared by wire cutting along the rolling direction (RD), diagonal direction (DD), and transverse direction (TD). The orientations and dimensions of the specimens are shown in Fig. 1.

2.2 Tensile Testing

High-temperature tensile tests were carried out on an MTS universal testing machine equipped with a high-temperature furnace. The specimens were mounted on high-temperature grips, and the tensile tests were conducted at room temperature (25°C), 720°C, 780°C, and 840°C. The tensile tests were performed under strain-controlled

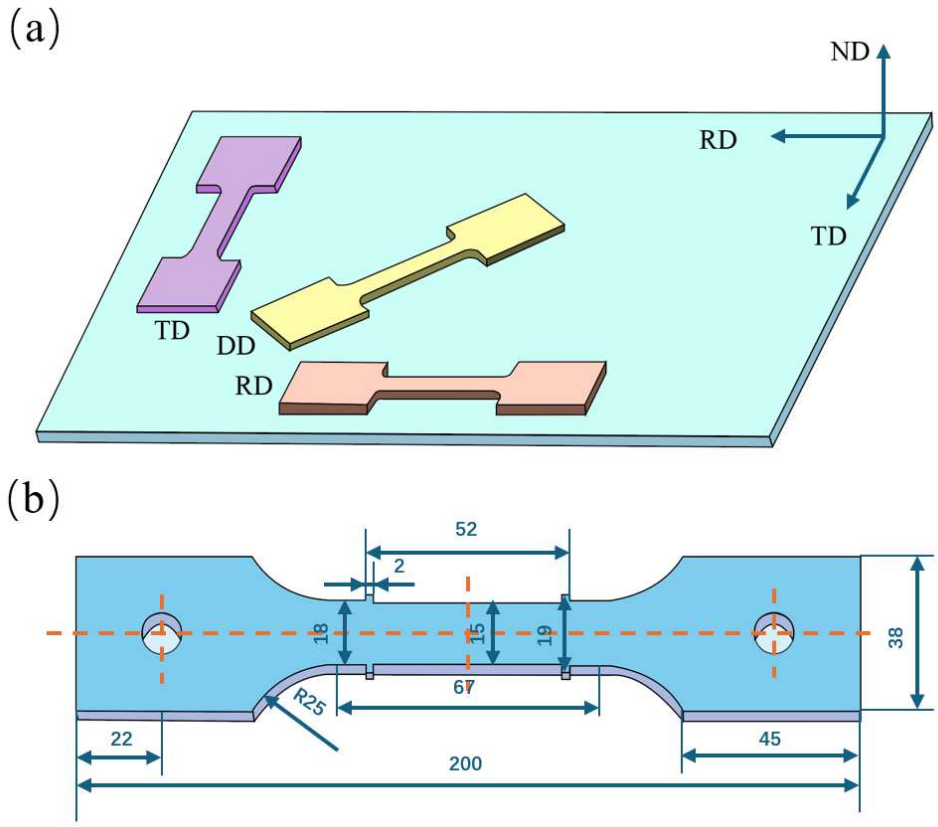


Fig. 1 Schematic diagram of (a) specimen dimensions and (b) orientations (Unit: mm)

conditions with a constant strain rate of $0.11min^{-1}$. During the tensile tests, the load–displacement data were automatically recorded by the computer system and subsequently converted into engineering stress-strain curves. For each temperature and loading direction, at least three valid tests were conducted to ensure the reliability of the experimental data.

2.3 Microstructural Characterization

Microstructural characterization was performed on the RD-TD plane of the specimen cross-section. The samples were mechanically polished using SiC abrasive papers of 240#, 400#, 800#, 1200#, and 2000#, followed by final polishing with diamond suspensions of 5 µm and 1 µm. Kroll's reagent (2% HF + 6% HNO_3 + 92% H_2O) was used as the etchant for metallographic observation, with an etching time of 10s. The etched metallographic samples were preliminarily observed using an OLYMPUS DSX510 optical microscope to characterize the overall microstructural morphology of the Ti60 sheet, the distribution of the α and β phases, and the size and orientation

of the primary α grains. For EBSD data acquisition, the samples were mechanically polished and subsequently subjected to ion milling for final surface preparation. The EBSD measurements were performed on a Tescan Maia3 scanning electron microscope equipped with an Oxford EBSD detector. The obtained data were analyzed using AZtecCrystal and HKL Technology Channel 5 software. For all EBSD measurements, the RD direction was defined as the x-axis, with the reference coordinate system designated as CS1 and the observation direction defined as Z1.

3 Results

3.1 High-Temperature Mechanical Properties and Anisotropy

The tensile strength and yield strength were extracted from the stress–strain curves (Fig. 2). The average tensile properties obtained along the three loading directions at different temperatures are shown in Fig. 3(a), where the error bars reflect the good repeatability and reliability of the experimental results. Fig. 3(b) shows the ratios of the values in the other directions relative to those in the TD direction under each condition, indicating significant variations in anisotropy. The experimental results indicate that the tensile properties of the alloy are highly sensitive to temperature and exhibit clear orientation dependence. With increasing testing temperature, both the yield strength and tensile strength along the three directions decrease monotonically, reflecting the typical high-temperature softening behavior of the material.

At room temperature, the yield strengths along the TD and RD directions are very close, with a difference of only 1.7 MPa. In contrast, the yield strength along the DD direction is lower, approximately 0.87 times that of the TD direction. At 720°C and 780°C, the yield strengths along all directions decrease significantly, while the order of TD>RD>DD is still maintained. However, the ratios of the RD and DD directions relative to the TD direction show larger deviations, indicating that the anisotropic behavior of the material changes within this temperature range. Notably, at 840°C, the mechanical properties exhibit a distinctive change: the yield strength along the DD direction becomes slightly higher than those along the RD and TD directions. The differences among the three directions become smaller, and the ranking even reverses to DD>RD>TD, indicating that the orientation dependence is significantly weakened at high temperature. Overall, the strength difference between the RD and TD directions is relatively small, whereas the DD direction exhibits a larger deviation compared with the other two directions. In addition, the yield strength shows lower sensitivity to the loading direction than the tensile strength.

3.2 Microstructural Characteristics

Fig. 4 shows the metallographic microstructure of the Ti60 sheet on the RD-TD plane. The grains exhibit a predominantly equiaxed morphology, consisting mainly of equiaxed α phase with a small amount of β phase. Fig. 4(a) shows the microstructure of the as-received sheet. The primary α grains are relatively uniformly distributed throughout the microstructure, and no obvious grain elongation along the rolling direction is observed, suggesting that the sheet underwent a moderate degree of rolling

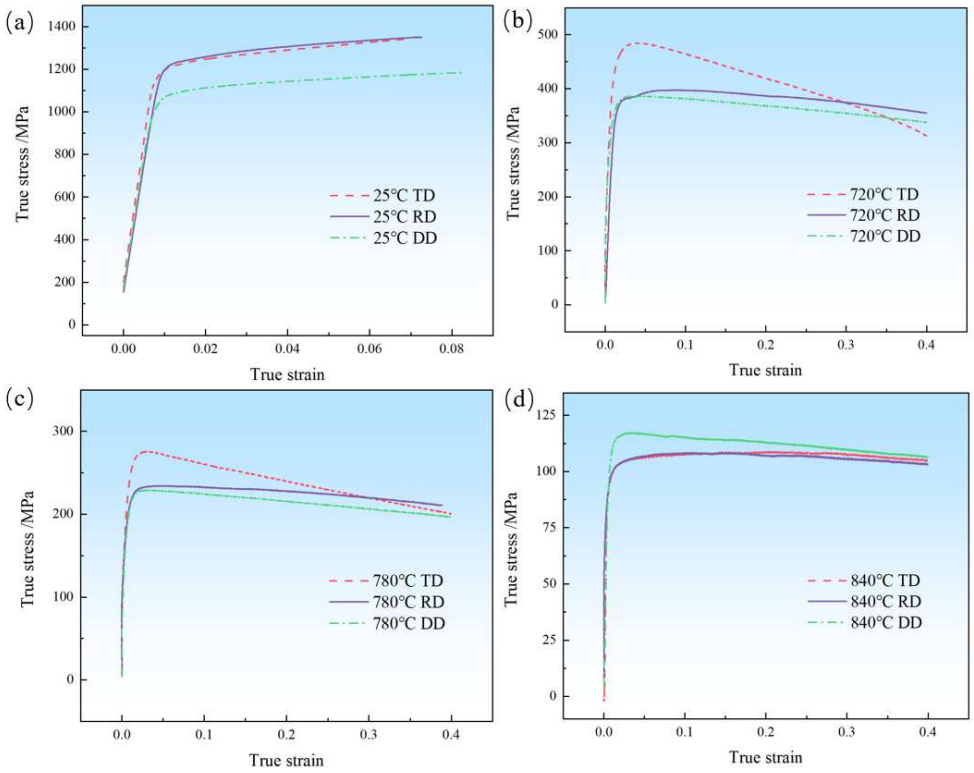


Fig. 2 True stress-strain curves of the Ti60 sheet at (a) 25°C, (b) 720°C, (c) 780°C, and (d) 840°C.

deformation or sufficient recrystallization. Table 1 summarizes the quantitative variations of the microstructural characteristics. The results indicate that with increasing temperature, the volume fraction of the α phase in the sheet gradually decreases, although the reduction is relatively small, remaining above 97%. Both the average area and the average equivalent circular diameter of the α phase exhibit an increasing trend. A clear three-stage variation can be observed. The average equivalent circular diameter of the α phase is 2.05 µm at 25°C, increases to approximately 2.77 µm at 720°C and 780°C, and further increases to 2.86 µm at 840°C. The average angle between the c-axis of the α grains and the x-axis is approximately 63°, whereas the average angle between the a-axis of the α grains and the x-axis is about 42°. The orientation angle varies with different temperature, exhibiting a clear three-stage variation. The average angle between the a-axis of the α grains and the x-axis is 37.87° at 25°C, increases to approximately 46.7° at 720°C and 780°C, and decreases to 41.63° at 840°C.

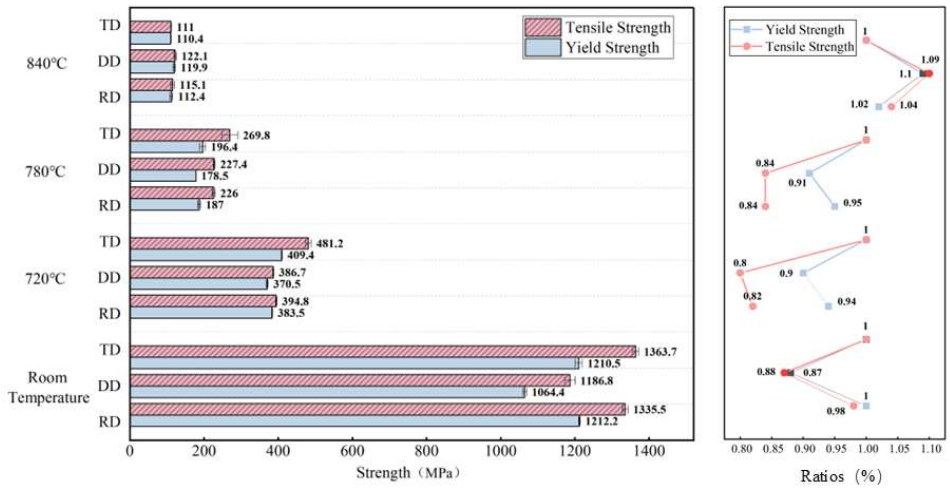


Fig. 3 Tensile properties and corresponding ratios of the Ti60 sheet at 25 °C, 720°C, 780°C, and 840°C: (a) average tensile properties, (b) ratios relative to the TD direction.

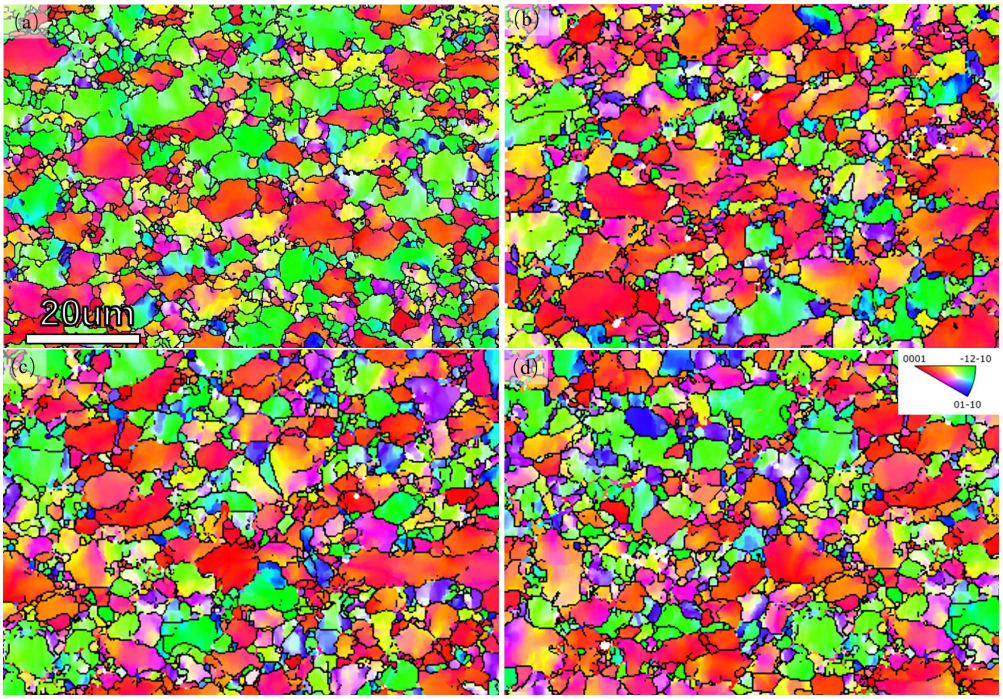


Fig. 4 Microstructural morphologies of the Ti60 sheet at (a) 25°C, (b) 720°C, (c) 780°C, and (d) 840°C.

Table 1 Microstructural size parameters of the Ti60 sheet.

Temperature	Volume fraction of the α phase	Average α phase area (μm^2)	Average equivalent diameter of α phase (µm)	Average c-axis angle of α grains relative to x-axis (°)	Average a-axis angle of α grains relative to x-axis (°)
25℃	99.50%	5.78	2.05	59.91	37.87
720℃	97.67%	9.45	2.76	65.66	46.51
780℃	98.10%	9.47	2.77	65.51	46.88
840℃	97.35%	9.98	2.86	64.71	41.63

4 Discussion

4.1 Anisotropic Behavior at Room Temperature

To explain the anisotropy of the macroscopic mechanical properties, a macroscopic texture analysis was carried out for the α phase (HCP structure). Fig. 5(a) shows the {0001}, {10-10}, and {11-20} pole figures of the α phase at room temperature calculated from EBSD data, which provide a comprehensive characterization of the texture features. The {0001} pole figure clearly shows that the α lamellae exhibit a pronounced c-axis orientation, mainly concentrated near the TD direction, forming a typical basal texture with a maximum texture intensity of 12.44 mrd. The {10-10} and {11-20} pole figures exhibit typical prismatic textures, although the texture intensity is relatively low. These two specific texture distributions directly determine the relative ease of activation of slip systems in grains during tensile loading along different directions. The Ti60 sheet already exhibits a certain degree of directional difference at room temperature, which mainly originates from the crystallographic texture formed during the rolling process and the non-uniform distribution of dislocations, leading to different activation conditions of effective slip systems along different directions.

To quantitatively verify the relationship between strength and slip system activation, the average Schmid factors of the dominant slip systems under uniaxial tension along the three sampling directions at room temperature were calculated, as shown in Fig 5(b). The slip systems considered in this study include basal slip $\{0001\}\langle 11-20\rangle$, prismatic slip $\{10\text{-}10\}\langle 11-20\rangle$, pyramidal $\langle a\rangle$ slip $\{10\text{-}11\}\langle 11-20\rangle$, and pyramidal $\langle c+a\rangle$ slip $\{11\text{-}22\}\langle -1-123\rangle$[31]. The average Schmid factors along different directions reflect the relative favorability of slip from a macroscopic perspective. The average Schmid factor for basal slip along the RD direction is only 0.19, indicating that basal slip is difficult to activate under tensile loading along the RD direction. e average Schmid factors for prismatic slip, pyramidal $\langle a\rangle$ slip, and pyramidal $\langle c+a\rangle$ slip along the RD direction are relatively high, with values of 0.44, 0.42, and 0.38, respectively. Along the TD direction, the average Schmid factors of all slip systems are relatively low, mainly ranging from 0.21 to 0.32. Among them, the values for pyramidal $\langle a\rangle$ slip and pyramidal $\langle c+a\rangle$ slip are slightly higher. Along the DD direction, the average Schmid factors of all slip systems are relatively high, mainly ranging from 0.30 to 0.42, among which pyramidal $\langle a\rangle$ slip exhibits the highest value. In summary,

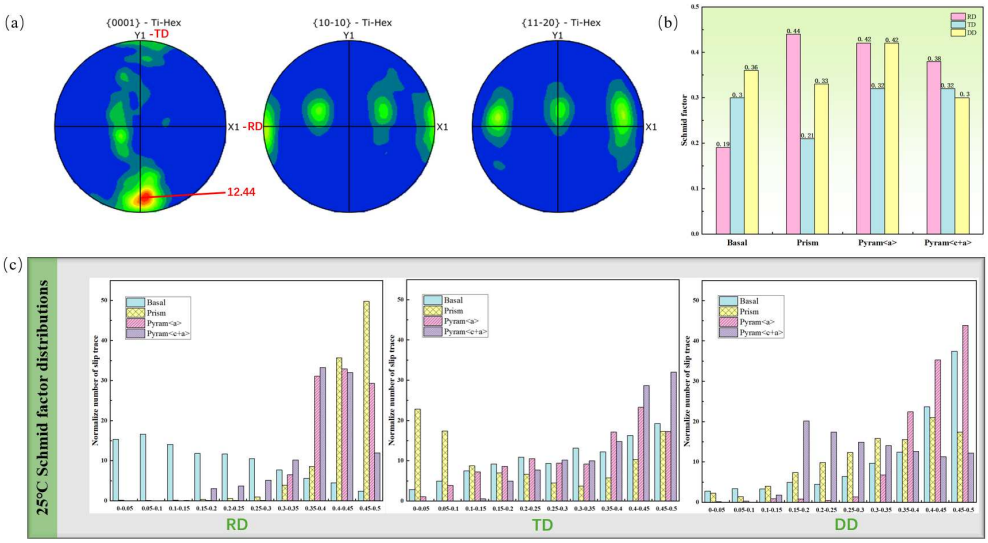


Fig. 5 (a) Pole figures, (b) average Schmid factors, and (c) histograms of Schmid factor distributions of the Ti60 sheet at 25°C

the RD direction provides the most favorable condition for the activation of prismatic slip and pyramidal $\langle a \rangle$ slip. Along the TD direction, the activation of all slip systems is relatively unfavorable, with deformation mainly dominated by pyramidal $\langle a \rangle$ slip and pyramidal $\langle c + a \rangle$ slip. Along the DD direction, all slip systems can be activated relatively easily, among which pyramidal $\langle a \rangle$ slip is the most readily activated.

The Schmid factor histograms reflect the distribution characteristics, dispersion, and the proportion of favorably oriented grains for slip of each slip system at the grain scale, as shown in Fig. 5(c). At room temperature, along the RD direction, the basal slip distribution is relatively dispersed and mainly located in the low Schmid factor range (0-0.2), indicating that the geometric condition for basal slip is unfavorable under tensile loading along the RD direction. Prismatic slip exhibits a pronounced peak in the 0.4-0.5 Schmid factor range, which is the highest among all slip systems, indicating a clear orientation advantage. Pyramidal $\langle a \rangle$ slip also occupies a relatively large proportion in the range of 0.35-0.5, second only to prismatic slip, but still showing a significant orientation advantage. Pyramidal $\langle c + a \rangle$ slip is mainly distributed in the Schmid factor range of 0.35-0.45, while still maintaining a relatively high proportion in other ranges; however, the number of grains in the high Schmid factor range remains limited. At room temperature, along the TD direction, the basal slip distribution is slightly shifted toward higher Schmid factor values compared with that along the RD direction; however, it remains relatively dispersed and thus does not play a dominant role. The distribution of prismatic slip shows higher frequencies in both the low and high Schmid factor ranges, while the intermediate range exhibits lower frequencies, leading to a more dispersed overall distribution. Pyramidal $\langle a \rangle$ slip extends toward the intermediate-to-high Schmid factor range (0.3-0.45), but the overall distribution

remains relatively dispersed. Pyramidal $\langle c+a \rangle$ slip is mainly concentrated in the range of 0.35-0.45, while its distribution also remains relatively dispersed. Along the TD direction, the distributions of all slip systems are relatively dispersed; however, pyramidal $\langle a \rangle$ slip and pyramidal $\langle c+a \rangle$ slip dominate compared with the other slip systems in this direction. At room temperature, along the DD direction, deformation is dominated by pyramidal $\langle a \rangle$ slip, which is mainly distributed in the Schmid factor range of 0.35-0.50 and exhibits a relatively concentrated distribution. In contrast, basal slip, prismatic slip, and pyramidal $\langle c+a \rangle$ slip exhibit more dispersed distributions, but are generally biased toward the intermediate-to-high Schmid factor range.

Whether a slip system is actually activated depends not only on the Schmid factor but also on whether the applied stress exceeds the critical resolved shear stress (CRSS) of that slip system under the given conditions[32]. In crystal plastic deformation, the yielding and early plastic response of the material are mainly governed by the slip systems that are activated first. When a loading direction exhibits a high Schmid factor and the corresponding slip system has a relatively low CRSS, the applied load can be more readily converted into effective resolved shear stress along that direction, thereby allowing slip to occur at a lower macroscopic stress level[33]. At room temperature, prismatic slip is the most easily activated slip mechanism in α-Ti and near-α titanium alloys, as it possesses the lowest CRSS. Therefore, it is often used as the normalization reference, with the CRSS of prismatic slip defined as $\mathrm{CRSS_{Prism}} = 1$[34]. Due to the strong solid-solution strengthening effect of alloying elements and the unfavorable dislocation dissociation mode, the CRSS of basal slip in titanium alloys at room temperature is higher than that of prismatic slip. However, studies by J. C. Williams and co-workers[35]have shown that with increasing Al concentration in titanium alloys, the activation of basal slip becomes progressively easier. When the Al content reaches 5-6%, the CRSS required to activate basal slip and prismatic slip becomes nearly comparable over a wide temperature range. Since the Al content in Ti60 reaches 5.7%, the CRSS of basal slip can reasonably be assumed as $\mathrm{CRSS_{Basal}} = 1.1$. Basal slip and prismatic slip are the two slip systems most readily activated in Ti60 at room temperature. Pyramidal $\langle a \rangle$ slip is the most difficult $\langle a \rangle$-type slip system to activate at room temperature, and its CRSS is generally 1-3 times that of prismatic slip. Taking the average value, the CRSS of pyramidal $\langle a \rangle$ slip can be set as $\mathrm{CRSS_{Pyram\langle a \rangle}} = 2$[36]. Pyramidal $\langle c+a \rangle$ slip requires simultaneous motion along both the a and c directions, and therefore usually does not participate in plastic deformation at room temperature. The CRSS of pyramidal $\langle c+a \rangle$ slip is typically about four times that of prismatic slip, and thus it can be assumed that $\mathrm{CRSS_{Pyram\langle c+a \rangle}} = 4$[37].

Based on the Schmid factor and CRSS, the activity of each slip system was quantitatively evaluated by introducing a slip activity parameter. For the $\langle a \rangle$-type slip systems, the expression is given as follows:

$$A^a(T) = \frac{S^a(T)}{C^a(T)} \tag{1}$$

where $A^a(T)$ represents the slip activity of the slip system at temperature T°C, $S^a(T)$ denotes the average Schmid factor of the slip system at temperature T, and $C^a(T)$ represents the CRSS of the slip system at temperature T. By substituting the room-temperature data into the above equation, the slip activity of each slip system

Table 2 Slip activities of different slip systems along various directions at room temperature.

Directions	Slip system	Slip activity A	summation
RD	Basal slip	0.17	0.92
	Prismatic slip	0.44	
	Pyramidal $\langle a \rangle$ slip	0.21	
	Pyramidal $\langle c+a \rangle$ slip	0.10	
TD	Basal slip	0.27	0.72
	Prismatic slip	0.21	
	Pyramidal $\langle a \rangle$ slip	0.16	
	Pyramidal $\langle c+a \rangle$ slip	0.08	
DD	Basal slip	0.33	0.94
	Prismatic slip	0.33	
	Pyramidal $\langle a \rangle$ slip	0.21	
	Pyramidal $\langle c+a \rangle$ slip	0.08	

can be obtained, as summarized in Table 2. A loading direction with higher slip activity generally corresponds to a lower macroscopic yield strength. At room temperature, the slip activity along different directions follows the order DD>RD>TD. Slip systems with lower slip activity require higher applied stress to initiate plastic slip, which consequently leads to the macroscopic strength ranking of TD>RD>DD. Combined with the pole figure analysis, the higher strength observed along the TD direction can be attributed to the fact that this direction is located at the most unfavorable position for slip activation relative to the crystallographic coordinate system. Microstructural characterization reveals that this anisotropy mainly originates from the strong crystallographic texture formed during the rolling process. The quantitative calculation of Schmid factors successfully correlates the macroscopic strength differences with crystallographic orientations, confirming that texture is the dominant factor leading to anisotropic behavior. Although the ranking obtained from the quantitative calculation of slip activity at room temperature can explain the ordering of yield strength, the yield strengths along the TD and RD directions are close to each other and both higher than that along the DD direction, whereas the slip activities of the DD and RD directions are comparable and lower than that of the TD direction. This indicates that, at room temperature, the plastic deformation of titanium alloys is not solely governed by slip, but also involves other dislocation activity mechanisms. For example, screw dislocations may alternately glide on multiple slip planes[38]. These non-thermally activated path mechanisms are not determined solely by a single Schmid activation condition; therefore, their activation weakens the macroscopic anisotropy induced by texture to a certain extent. That is, plastic deformation of the titanium alloy at room temperature is mainly dominated by $\langle a \rangle$ slip, in combination with non-thermally activated path mechanisms.

4.2 Anisotropy Analysis at Intermediate and High Temperatures

Figs. 6(a) and (d) show the {0001}, {10-10}, and {11-20} pole figures of the α phase at 720°C and 780°C. It is observed that when the temperature increases to 720°C, the

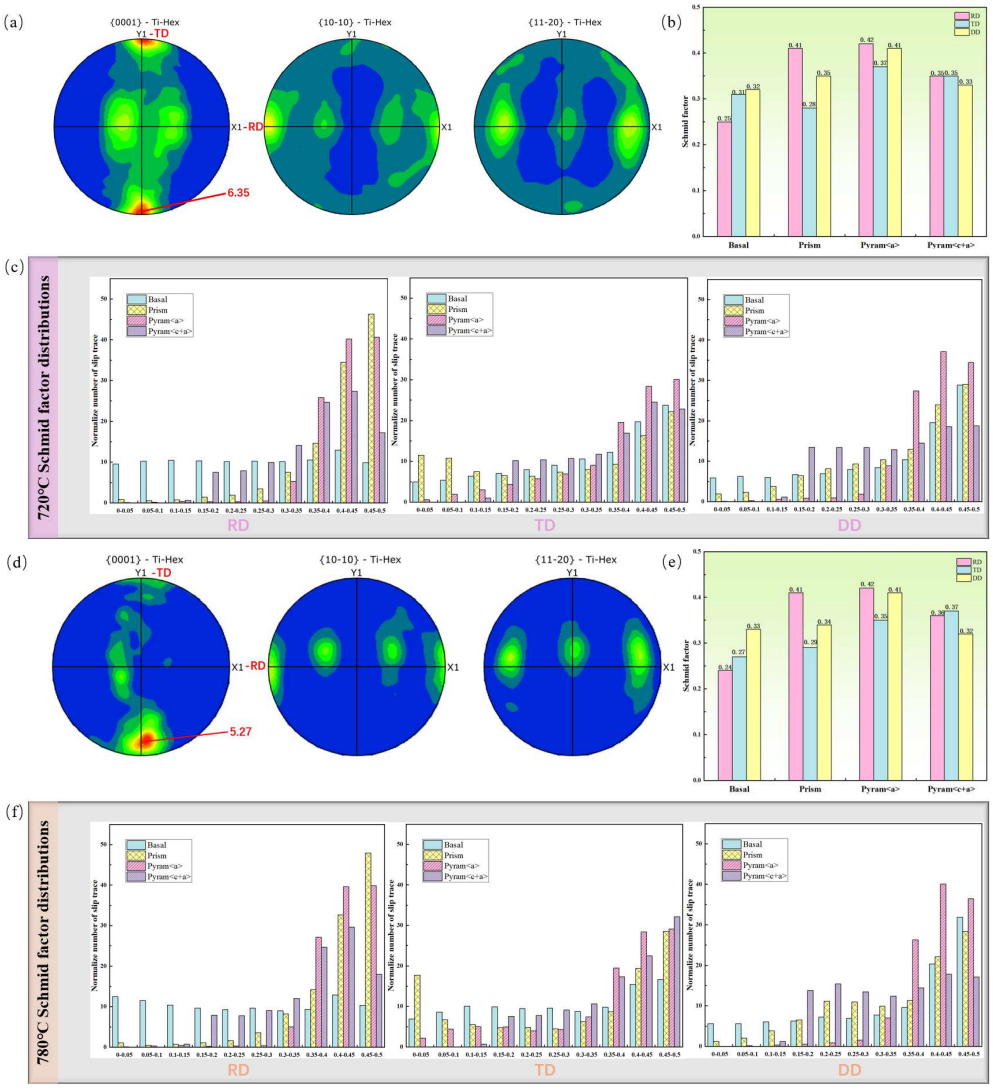


Fig. 6 (a) Pole figures at 720°C, (b) average Schmid factors at 720°C, (c) histograms of Schmid factor distributions at 720°C, (d) pole figures at 780°C, (e) average Schmid factors at 780°C, and (f) histograms of Schmid factor distributions at 780°C.

maximum texture intensity decreases, and the grains in the pole figures are mainly aligned parallel to the positive and negative TD directions, forming a typical double-peak texture. When the temperature increases to 780°C, the texture intensity becomes weaker, while the overall pole distribution remains essentially unchanged.

Figs. 6(b) and (e) show the average Schmid factors of the dominant slip systems at 720°C and 780°C. After the temperature rises to the intermediate and high-temperature range, along the RD direction, the average Schmid factor for basal slip

increases to some extent; however, this slip system is still difficult to activate, with a value of approximately 0.25. The average Schmid factors for prismatic slip and pyramidal $\langle c + a \rangle$ slip show slight decreases, from 0.44 to 0.41 and from 0.38 to 0.36, respectively. The average Schmid factor for prismatic slip still remains at 0.42, showing essentially no change. Along the TD direction, the average Schmid factor for basal slip exhibits a fluctuating variation with increasing temperature, with an average value of approximately 0.30. The average Schmid factors for prismatic slip, pyramidal slip, and pyramidal $\langle c+a \rangle$ slip all increase slightly with increasing temperature, indicating that slip activation along the TD direction in the intermediate to high-temperature range becomes easier than at room temperature, although the corresponding values remain lower than those along the other directions. Along the DD direction, compared with room temperature, the average Schmid factors for basal slip and pyramidal $\langle a \rangle$ slip decrease slightly, whereas those for prismatic slip and pyramidal $\langle c + a \rangle$ slip increase slightly. Nevertheless, the average Schmid factors of all slip systems remain at relatively high levels. Figs. 6(c) and (f) show the histograms of Schmid factor distributions at 720°C and 780°C. Along the RD direction, the distribution of basal slip gradually becomes more uniform with increasing temperature, indicating that the geometric condition for basal slip along the RD direction remains unfavorable, although the geometric constraint on basal slip is slightly alleviated as the temperature increases. Prismatic slip and pyramidal $\langle a \rangle$ slip occupy relatively large proportions in the Schmid factor range of 0.35–0.50, indicating clear advantages in activation. Pyramidal $\langle c + a \rangle$ slip is mainly distributed in the range of 0.35–0.45, and its distribution is more dispersed than those of prismatic slip and pyramidal $\langle a \rangle$ slip. Along the TD direction, the distributions of all slip systems are relatively uniform; however, with increasing temperature, they show a tendency to shift toward higher Schmid factor values. Compared with the other slip systems, pyramidal $\langle a \rangle$ slip and pyramidal $\langle c + a \rangle$ slip still occupy a dominant position in this direction. Along the DD direction, deformation is still dominated by pyramidal $\langle a \rangle$ slip after the temperature increases, while basal slip, prismatic slip, and pyramidal $\langle c+a \rangle$ slip remain distributed in the intermediate-to-high Schmid factor range.

In the intermediate temperature range of 720-780°C, the CRSS of all slip systems decreases significantly, which is attributed to the enhancement of thermally activated dislocation motion and the reduction of dislocation pile-up. However, the rates at which the CRSS values of different slip systems decrease with increasing temperature differ markedly. The CRSS of $\langle a \rangle$-type slip systems decreases significantly with increasing temperature, and the differences among the three are markedly reduced, allowing the three slip systems to become simultaneously active[39]. Although the CRSS of pyramidal $\langle c+a \rangle$ slip decreases most significantly, it still remains the highest in absolute value. Therefore, when the CRSS differences among the three $\langle a \rangle$-type slip systems are reduced, the summed Schmid factors of the $\langle a \rangle$-type slip systems along the TD direction become the lowest, whereas the difference in the summed Schmid factors between the RD and DD directions is very small. This leads to comparable yield strengths along the DD and RD directions at 720-780°C, both of which are lower than that along the TD direction.Within this temperature range, plastic deformation relies

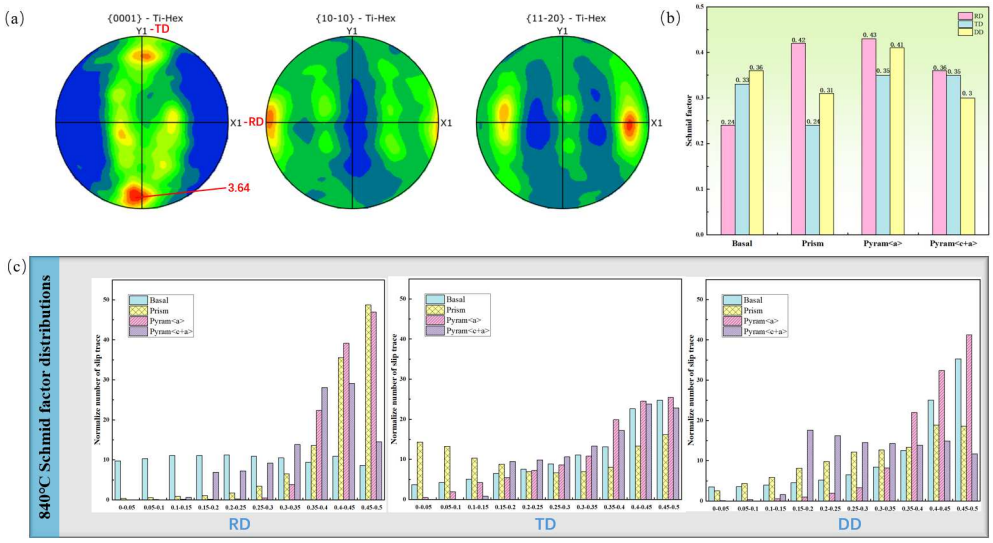


Fig. 7 (a) pole figures, (b) average Schmid factors, and (c) histograms of Schmid factor distributions at 840°C.

more strongly on thermally activated dislocation slip. For grains with different orientations, the thermally activated energy barriers of the dominant slip systems differ, which further amplifies the anisotropy induced by the initial crystallographic texture. Plastic deformation within this temperature range depends more strongly on the activation of slip systems than at room temperature, and the yield strength is therefore more strongly governed by slip-system activity than under room-temperature conditions. As a result, the decrease in the RD/TD ratio is observed in this temperature range.

4.3 Anisotropy Analysis at High Temperature

Fig. 7(a) shows the{0001}, {10-10}, and{11-20} pole figures of the α phase at 840°C. The texture intensity decreases to 3.74 mrd. Although a preferred orientation is still retained, the distribution becomes more diffuse. Figs. 7(b) and (c) show the average Schmid factors and the histograms of Schmid factor distributions at 840°C, respectively. It can be observed that, after the temperature increases, the values of all slip systems along each direction change only slightly.

When the temperature increases to the high-temperature region of 840°C, the anisotropy exhibits a significant change. The yield strength along the TD direction is no longer the highest, and the yield strength along the DD direction is no longer the lowest, indicating a reversal in the yield strength ranking. This indicates that, at high temperatures, the deformation mechanism undergoes a fundamental change, weakening the dominant role of crystallographic orientation. At elevated temperatures, deformation is no longer solely governed by intragranular slip; instead, grain boundaries gradually undergo relative sliding and cooperative migration[40]. Fig. 8(a)

and (b) shows the kernel average misorientation (KAM) maps of Ti60 at 720°C and 840°C, which serve as a quantitative indicator of the intragranular orientation gradient and essentially reflect the density of geometrically necessary dislocations (GNDs) [41]. At 720°C, the average KAM value of the sheet is 1.28°, whereas it decreases to 1.15° when the temperature increases to 840°C. With increasing temperature, the KAM value decreases, indicating a reduction in the intragranular orientation gradient and a corresponding decrease in GND density. This suggests that dislocation activity is suppressed, while the proportion of grains behaving closer to rigid bodies increases, which is conducive to grain boundary sliding[42]. Fig. 8(c) and (d) shows the maps of low-angle grain boundaries (LAGBs) and high-angle grain boundaries (HAGBs) of Ti60 at 720°C and 840°C. With increasing temperature, the fraction of high-angle grain boundaries (HAGBs: GB>15°) increases, while the fraction of low-angle grain boundaries (LAGBs: 2°<GB<15°) decreases. LAGBs can be regarded as "storage sites" for dislocations, whereas HAGBs act as "channels" for grain boundary sliding. The decrease in LAGBs indicates a reduction in dislocation activity, while the increase in HAGBs provides favorable interfacial conditions for grain boundary sliding[43]. According to the data in Table 2, the average angle between the a-axis of the α grains and the loading direction decreases from 46.51° to 41.63°, indicating that a systematic reorientation of the grains has occurred. This reorientation is accompanied by a decrease in KAM and an increase in the fraction of high-angle grain boundaries, indicating that grains tend to participate in deformation in a quasi-rigid-body manner. Plastic deformation is thus accommodated through grain boundary–dominated cooperative mechanisms, in which grain boundary sliding may play an important role. Grain boundary sliding is relatively insensitive to crystallographic orientation and shows a weak dependence on the Schmid factor and CRSS. Its activation further promotes deformation homogenization and reduces the influence of crystallographic texture[44, 45].

At elevated temperatures, the CRSS of pyramidal $\langle c+a \rangle$ slip decreases significantly. The $\langle c+a \rangle$ slip provides a strain component along the c-axis direction, which cannot be accommodated by $\langle a \rangle$ slip. Because pyramidal $\langle c+a \rangle$ slip provides a larger number of available slip systems, its activation significantly enhances the multiple-slip capability of the material. As a result, even grains with hard orientations that are unfavorable for $\langle a \rangle$ slip can accommodate deformation through the activation of $\langle c+a \rangle$ slip. This diversification of deformation modes effectively homogenizes the deformation capability among grains with different orientations, thereby leading to a reduction in anisotropy. At 840°C, the DD direction exhibits the highest strength, while the tensile properties along the RD direction are slightly higher than those along the TD direction. This ranking is consistent with the order of the average Schmid factors for pyramidal $\langle c+a \rangle$ slip at 840°C, where TD is slightly higher than RD, followed by DD. The deformation mechanism dominated by grain boundary sliding, accompanied by the simultaneous activation of multiple dislocation slip systems, leads to the reversal of yield strength anisotropy at 840°C.

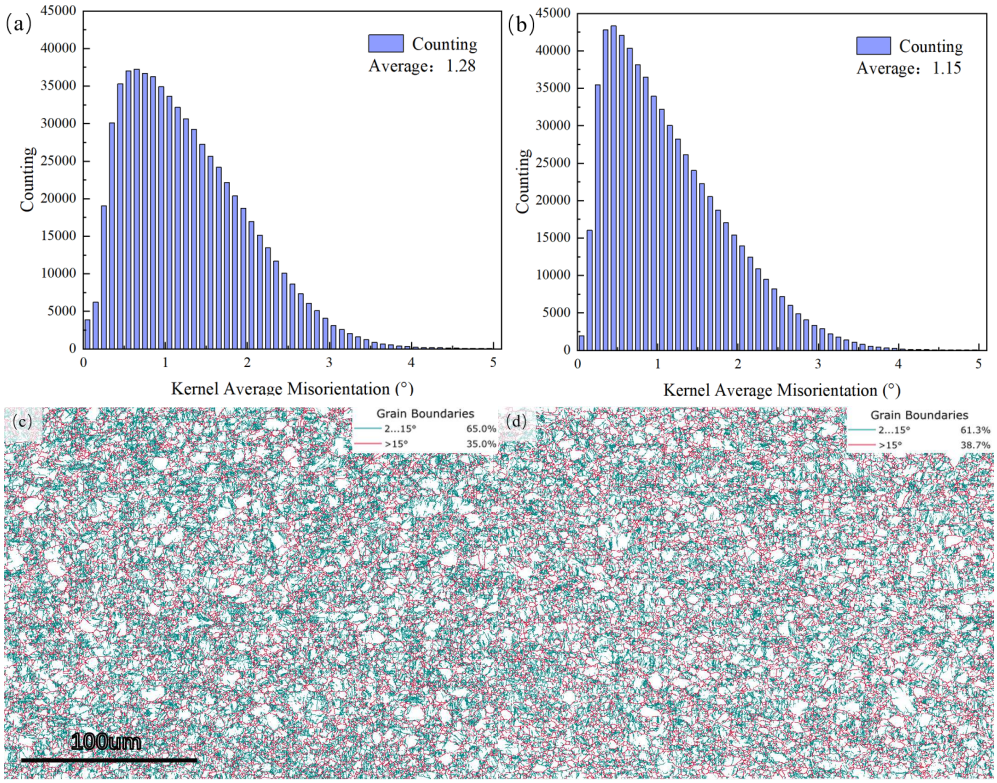


Fig. 8 (a) KAM distribution histogram at 720°C, (b) KAM distribution histogram at 840°C, (c) grain boundary map at 720°C, and (d) grain boundary map at 840°C of the Ti60 sheet.

5 Conclusion

1. The yield strength of the Ti60 rolled sheet exhibits pronounced mechanical anisotropy, which can be divided into three distinct stages: At room temperature, the yield strengths along the TD and RD directions are comparable and higher than that along the DD direction, following the order TD>RD>DD. In the temperature range of 720-780°C, the yield strengths along the RD and DD directions are comparable and lower than that along the TD direction, maintaining the order of TD>RD>DD. At 840°C, the yield strengths along the TD and RD directions are comparable and lower than that along the DD direction, indicating a reversal in the ranking, with DD>RD>TD.

2. At room temperature, the plastic behavior of the titanium alloy is mainly governed by prismatic slip and basal slip. The ranking of slip activity, jointly determined by the Schmid factor and CRSS, follows the order DD>RD>TD. Non-thermally activated path mechanisms weaken the macroscopic anisotropy induced by crystallographic texture to a certain extent. The anisotropy of the titanium alloy at

room temperature is mainly governed by $\langle a \rangle$ slip, in combination with non-thermally activated path mechanisms.

3. In the intermediate temperature range of 720-780°C, plastic deformation becomes more dependent on thermally activated dislocation slip, and the CRSS of each slip system decreases significantly, although the rates of decrease differ. The CRSS differences among $\langle a \rangle$-type slip systems are significantly reduced, allowing multiple $\langle a \rangle$-type slip systems to participate in deformation simultaneously. In the intermediate-temperature range, the proportion of non-thermally activated slip is reduced, while the dominance of dislocation slip is enhanced. This results in a strong negative correlation between yield strength and dislocation slip activity, causing the yield strength along the RD direction to decrease to a level comparable to that along the DD direction.

4. When the temperature rises to 840°C, the dominant deformation mechanism undergoes a fundamental change. The change in the intergranular orientation angles of the α grains, the decrease in KAM values, and the increase in the fraction of HAGBs collectively indicate that the dominant deformation mechanism shifts to grain boundary sliding. The CRSS of pyramidal $\langle c+a \rangle$ slip decreases significantly and is extensively activated. The c-axis plastic deformation capability it provides markedly enhances the multiple-slip coordination of the material, making the deformation capability among grains with different orientations more consistent and thereby significantly reducing anisotropy. The deformation mechanism dominated by grain boundary sliding, accompanied by the simultaneous activation of multiple dislocation slip systems, leads to the reversal of yield strength anisotropy at 840°C.

Acknowledgements. 1.National Natural Science Foundation of China(No: 52475388). 2.Liaoning Revitalization Talents Program(XLYC2403146) 3.Fundamental Research Funds for The Universities of Liaoning Province(No. LJ232510143010)

References

[1] Williams, J.C., Boyer, R.R.: Opportunities and issues in the application of titanium alloys for aerospace components. Metals **10**(6), 705 (2020)

[2] Pagan, D.C., Bernier, J.V., Dale, D., Ko, J.P., Turner, T.J., Blank, B., Shade, P.A.: Measuring ti-7al slip system strengths at elevated temperature using high-energy x-ray diffraction. Scripta Materialia **142**, 96–100 (2018)

[3] Dai, Y., Xiao, Y., Zeng, W., Jia, R., Jia, W.: Mechanism of crystallographic orientation and texture evolution of ti60 alloy during plane strain compression. Metals **14**(3), 359 (2024)

[4] Wu, Y., Fan, R., Chen, M., Wang, K., Zhao, J., Xiao, W.: High-temperature anisotropic behaviors and microstructure evolution mechanisms of a near-α ti-alloy sheet. Materials Science & Engineering: A **820**, 141560 (2021)

[5] Kumar, P.S.R., Mashinini, P.M.: Titanium alloys for aerospace structures and engines. In: Aerospace Materials, pp. 227–253. Elsevier, Amsterdam (2025)

[6] Kuczyńska-Zemła, D., Lucas, M.M., Lavisse, L., Zemła, M., Herbst, F., Pacorel, V., Kwaśniak, P.: Microstructural influence on high-temperature oxidation of near-α titanium alloys: Timetal 834 and 6242s. Corrosion Science **255**, 113081 (2025)

[7] Wanjara, P., Jahazi, M., Monajati, H., Yue, S.: Influence of thermomechanical processing on microstructural evolution in near-α alloy imi834. Materials Science & Engineering: A **416**(1-2), 300–311 (2006)

[8] Tang, J., Wang, Y., Wang, S., Cai, M., Xu, Z.: Composition design and microstructure optimization of a metastable β-type titanium alloy with ultra-high strength. Advanced Engineering Materials **27**(7), 2402099–2402099 (2025) https://doi.org/10.1002/ADEM.202402099

[9] Dong, S., Gong, Z., Chen, Z., Qu, Y., Chen, R., Liu, S., Li, G.: High temperature tensile creep behavior and microstructure evolution of ti60 alloy rolled sheet. Materials Today Communications **41**, 110805–110805 (2024) https://doi.org/10.1016/J.MTCOMM.2024.110805

[10] Wu, T., Gao, Z., Chen, M., Dong, H.: Data-driven time series analysis for high-temperature deformation behavior prediction based on the deep learning approach: A case study on titanium alloy. Journal of Alloys and Compounds **1037**, 182233–182233 (2025) https://doi.org/10.1016/J.JALLCOM.2025.182233

[11] Yang, X., Shen, D., Wang, Q., Su, Y., Liu, Y., Guo, Z., Xiong, R., Meng, Y., Feng, Z., Hao, S., Ma, T., Li, W.: Microstructure control and high-temperature mechanical response of ta15 titanium alloy fabricated by selective laser melting. Materials Today Communications **49**, 114072–114072 (2025) https://doi.org/10.1016/J.MTCOMM.2025.114072

[12] Materials selection of optimized titanium alloys for aircraft applications. Materials Research **21**(2) (2018)

[13] Ma, X.Z., Xiang, Z.L., Ma, M.Z., Cui, Y.P., Ren, W.M., Wang, Z.T., Huang, J.C., Chen, Z.Y.: Investigation of microstructures, textures, mechanical properties and fracture behaviors of a newly developed near α titanium alloy. Materials Science & Engineering A **775**, 138996–138996 (2020) https://doi.org/10.1016/j.msea.2020.138996

[14] Le, C., Zihao, M., Binbin, Z., Changyu, Z., Xiaohua, H.: Understanding the anisotropic tensile deformation behavior of commercially pure titanium by experiments and crystal plasticity simulations. Materials Letters **339** (2023) https://doi.org/10.1016/J.MATLET.2023.134095

[15] Zhang, B., Zhao, Z., Wang, Q., Liu, J., Yang, R.: The effect of deformation temperature on the microstructure and crystallographic orientation evolution of ti60 alloy after annealing. Materials Science & Engineering: A **880**, 145360 (2023)

[16] Z.B.Zhao, Z.Liu, Q.J.Wang, J.R.Liu, R.Yang: Analysis of local crystallographic orientation in an annealed ti60 billet. Journal of Materials Science & Technology **35**(04), 591–595 (2019)

[17] Li, W., Chen, Z., Liu, J., Zhu, S., Sui, G., Wang, Q.: Rolling texture and its effect on tensile property of a near-α titanium alloy ti60 plate. Journal of Materials Science & Technology **35**(05), 790–798 (2019)

[18] Li, W., Chen, Z., Liu, J., Wang, Q., Sui, G.: Effect of texture on anisotropy at 600°c in a near-α titanium alloy ti60 plate. Materials Science & Engineering A **688**, 322–329 (2017) https://doi.org/10.1016/j.msea.2017.01.098

[19] Liu, S., Niu, H., Liu, J., Cao, P., Yang, W.: Coupling effects of interlayer holes and α-ti variants on mechanical properties and anisotropy of additively manufactured titanium alloy. Materials Characterization **223**, 114954–114954 (2025) https://doi.org/10.1016/J.MATCHAR.2025.114954

[20] Yu, W., Lv, Y., Li, S., Wang, Y., Li, B., Liao, Z.: Mechanism of the anisotropy of yield ratio in ta5 titanium alloy plates. Materials Science & Engineering A **639**, 314–319 (2015) https://doi.org/10.1016/j.msea.2015.04.083

[21] Yanli, L., Yifan, W., Yibo, S., Junpeng, L., Kelin, C., Zhubin, H.: Identification of anisotropic coefficients in the non-principal axis directions of tubular materials using hole bulging test. Materials (Basel, Switzerland) **16**(13) (2023) https://doi.org/10.3390/MA16134629

[22] Li, B., Fan, J., Zhang, W., Zhao, J., Zhao, D., Tao, H., Hao, X., Wang, F., Jiang, P., Kou, H., Li, J.: Texture evolution and anisotropy of ta18 titanium alloy strip under rolling and heat treatment conditions. Journal of Materials Research and Technology **34**, 1582–1590 (2025) https://doi.org/10.1016/J.JMRT.2024.12.142

[23] Wei, L., Songsong, L., Hui, Y.: Research on the anisotropy of plastic behavior and deformation mechanism of textured pure titanium. Materials Characterization **194** (2022) https://doi.org/10.1016/J.MATCHAR.2022.112483

[24] Behnam, A., Orestis, P., William, V.H., M., H.J., J., B.I., Christos, T.: Data-driven texture design for reducing elastic and plastic anisotropy in titanium alloys. Acta Materialia **265**, 119585 (2024) https://doi.org/10.1016/J.ACTAMAT.2023.119585

[25] Yong, W., Ronglei, F., Minghe, C., Kehuan, W., Jie, Z., Wenchao, X.: High-temperature anisotropic behaviors and microstructure evolution mechanisms of a near-α ti-alloy sheet. Materials Science & Engineering A **820** (2021) https://doi.org/10.1016/J.MSEA.2021.141560

[26] Guo, B., Gao, H., Kong, C., Wang, Z., Cui, H., Yu, H.: Transverse texture weakening and anisotropy improvement of ti-6al-4v alloy sheet via asymmetric rolling

and static recrystallization annealing. Journal of Alloys and Compounds **1010**, 177507–177507 (2025) https://doi.org/10.1016/J.JALLCOM.2024.177507

[27] Li, Y., Gao, P., Yu, J., Jin, S., Chen, S., Zhan, M.: Mesoscale deformation mechanisms in relation with slip and grain boundary sliding in ta15 titanium alloy during tensile deformation. Journal of Materials Science & Technology **98**(03), 72–86 (2022)

[28] Qi, Q., Zheng-qing, L., Yong, J., Yi-ren, W., Xing-long, A., Min, S.: Basal stacking fault induced twin boundary gliding, twinning disconnection and twin growth in hcp ti from the first-principles. Transactions of Nonferrous Metals Society of China **31**(2), 382–390 (2021) https://doi.org/10.1016/S1003-6326(21)65503-6

[29] Furuhara, T., Poorganji, B., Abe, H., Maki, T.: Dynamic recovery and recrystallization in titanium alloys by hot deformation. JOM **59**(1), 64–67 (2007) https://doi.org/10.1007/s11837-007-0013-8

[30] Wang, Y., Li, Z., Wang, H., Hou, M., Yu, K., Xu, Y., Xiao, H.: Flow behavior and dynamic recrystallization mechanism of a new near-alpha titanium alloy ti-0.3mo-0.8ni-2al-1.5zr. Journal of Materials Research and Technology **30**, 3863–3876 (2024) https://doi.org/10.1016/J.JMRT.2024.04.076

[31] Wang, K., Li, H., Zhou, Y., Wang, J., Xin, R., Liu, Q.: Dislocation slip and crack nucleation mechanism in dual-phase microstructure of titanium alloys: A review. Acta Metallurgica Sinica (English Letters) **36**(3), 353–365 (2023) https://doi.org/10.1007/S40195-022-01505-4

[32] Kawano, Y., Sato, M., Mayama, T., Mitsuhara, M., Yamasaki, S.: Quantitative evaluation of slip activity in polycrystalline α-titanium considering non-local interactions between crystal grains. International Journal of Plasticity **127**, 102638–102638 (2020) https://doi.org/10.1016/j.ijplas.2019.12.001

[33] Hémery, S., Ali, A.N., Smerdova, O., Tromas, C.: Deformation mechanisms in the α phase of the ti-6al-2sn-4zr-2mo titanium alloy: In situ experiments and simulations. International Journal of Plasticity **175**, 103947 (2024) https://doi.org/10.1016/J.IJPLAS.2024.103947

[34] Wang, L., Zheng, Z., Phukan, H., Kenesei, P., Park, J.-S., Lind, J., Suter, R.M., Bieler, T.R.: Direct measurement of critical resolved shear stress of prismatic and basal slip in polycrystalline ti using high energy x-ray diffraction microscopy. Acta Materialia **132**, 598–610 (2017) https://doi.org/10.1016/j.actamat.2017.05.015

[35] Williams, J.C., Baggerly, R.G., Paton, N.E.: Deformation behavior of hcp ti-al alloy single crystals. Metallurgical and Materials Transactions, A. Physical Metallurgy and Materials Science **33**(3), 837–850 (2002) https://doi.org/10.1007/s11661-002-0153-y

[36] Li, H., Mason, D.E., Bieler, T.R., Boehlert, C.J., Crimp, M.A.: Methodology for estimating the critical resolved shear stress ratios of α-phase ti using ebsd-based trace analysis. Acta Materialia **61**(20), 7555–7567 (2013) https://doi.org/10.1016/j.actamat.2013.08.042

[37] Hémery, S., Villechaise, P., Banerjee, D.: Microplasticity at room temperature in α/β titanium alloys. Metallurgical and Materials Transactions A **51**(10), 4931–4969 (2020)

[38] Rida, A., Rao, S.I., El-Awady, J.A.: Characteristics of ¡a¿ screw dislocations and their slip on prismatic and pyramidal planes in pure α titanium from atomistic simulations. Materialia **24**, 101503 (2022)

[39] Li, H., Li, C., Chen, D., Liu, Y., Zhao, Z., Zhang, B., Qi, M., Liu, J., Wang, Q.: Temperature-dependent deformation mechanisms in ti65 alloy: An in situ tensile study. Materials **18**(14), 3270–3270 (2025) https://doi.org/10.3390/MA18143270

[40] Hémery, S., Tromas, C., Villechaise, P.: Slip-stimulated grain boundary sliding in ti-6al-4v at room temperature. Materialia **5**, 100189 (2019)

[41] Rui, S.-S., Han, Q.-N., Wang, X., Li, S., Ma, X., Su, Y., Cai, Z., Du, D., Shi, H.-J.: Correlations between two ebsd-based metrics kernel average misorientation and image quality on indicating dislocations of near-failure low alloy steels induced by tensile and cyclic deformations. Materials Today Communications **27**, 102445 (2021)

[42] Zhou, J., Wu, M., Zhang, W., Ning, J.: High-temperature deformation behaviors of gradient-structured mg-gd-y-zr alloys at high strain rates. Materials **18**(17), 4085 (2025)

[43] Liang, C., Wang, N., Chen, Y., Jiang, C., Wu, G., Zhao, Q., Zhu, L., Luo, J.: Transition of low and high-angle grain boundaries during strain rate-induced dislocation storage and annihilation. Materials Characterization **205**, 113284 (2023)

[44] Zhao, Y., Toth, L.S., Massion, R., Skrotzki, W.: Role of grain boundary sliding in texture evolution for nanoplasticity. Advanced Engineering Materials **20**(4), (2018) https://doi.org/10.1002/adem.201700212

[45] Langdon, T.G.: Grain boundary sliding revisited: Developments in sliding over four decades. Journal of Materials Science **41**(3), 597–609 (2006) https://doi.org/10.1007/s10853-006-6476-0